Boulder Stranding in Ejecta Launched by an Impact Generated Seismic Pulse

Esteban Wright[a,*], Alice C. Quillen[a], Juliana South[a], Randal C. Nelson[b],
Paul Sánchez[c], Larkin Martini[a,d], Stephen R. Schwartz[e,f], Miki Nakajima[a,g],
Erik Asphaug[e]

[a]*Department of Physics and Astronomy, University of Rochester, Rochester, NY 14627, USA*
[b]*Department of Computer Science, University of Rochester, Rochester, NY 14627, USA*
[c]*Colorado Center for Astrodynamics Research, The University of Colorado Boulder, UCB 431, Boulder, CO 80309-0431, United States*
[d]*Department of Geology and Geological Engineering, Colorado School of Mines, Golden, CO 80401, USA*
[e]*Lunar and Planetary Lab, University of Arizona, Tucson, AZ, USA*
[f]*Laboratoire Lagrange, Université Côte d'Azur, Observatoire de la Côte d'Azur, CNRS, C.S. 34229, 06304 Nice Cedex 4, France*
[g]*Department of Earth and Environmental Sciences, University of Rochester, Rochester, NY 14627, USA*

Abstract

We consider how an impact generated seismic pulse affects the surface of an asteroid distant from the impact site. With laboratory experiments on dry polydisperse gravel mixtures, we track the trajectories of particles ejected from the surface by a single strong upward propagating pressure pulse. High speed video images show that ejecta trajectories are independent of particle size, and collisions primarily take place upon landing. When they land particles are ballistically sorted, as proposed by Shinbrot et al. (2017), leaving larger particles on the surface and smaller particles more widely dispersed. A single strong pulse can leave previously buried boulders stranded on the surface. Boulder stranding due to an impact excited seismic pulse is an additional mechanism that could leave large boulders present on the surface of rubble asteroids such as 162173 Ryugu, 101955 Bennu and 25143 Itokawa.

*Corresponding author, ewrig15@ur.rochester.edu

1. Introduction

Particle size segregation on rubble covered asteroids such as 25143 Itokawa and the presence of large boulders on the surface are usually explained with the Brazil nut effect (BNE) (Matsumura et al., 2014; Perera et al., 2016), by which vibrations in the presence of gravity slowly propel larger particles to the surface. In the case of 25143 Itokawa, the size distribution seems to be correlated to the total gravitational potential with large and small boulders in regions of high and low potential respectively (Tancredi et al., 2015; Miyamoto et al., 2007). The Brazil nut effect brings the largest nuts in a shaken bowl of mixed nuts to the top (e.g., Rosato et al. 1987), and is responsible for the appearance of boulders in agricultural fields after repeated cycles of frost heave. The Brazil nut effect is mediated through a number of possible mechanisms (e.g. ratcheting, convection), all dependent on gravitational acceleration. Smaller particles percolate or slip beneath larger ones and ratchet the largest ones upward (Williams, 1976; Rosato et al., 1987; Jullien et al., 1992; Hong et al., 2001; Maurel et al., 2017). Alternatively a convection pattern dredges particles up to the surface, but inhibits larger particles from sinking (Knight et al., 1993; Chujo et al., 2018; Matsumura et al., 2014).

Impact induced seismicity is important on small asteroids due to their low surface gravity and small volume which limits vibrational energy dispersal (Cintala et al., 1978; Cheng et al., 2002; Richardson et al., 2004). Seismic disturbances can destabilize loose material resting on slopes, causing landslides (Titley, 1966), and crater degradation and crater erasure (Richardson et al., 2004; Thomas and Robinson, 2005; Richardson et al., 2005; Asphaug, 2008; Yamada et al., 2016). Regions of different crater densities on asteroid 433 Eros can be explained by strong impacts that erase craters (Thomas and Robinson, 2005).

Unfortunately, little is currently known about how impact generated seismic waves are excited, dispersed, attenuated and scattered in asteroids. The rapidly attenuated seismic pulse or 'jolt' model (Nolan et al., 1992; Greenberg et al., 1994, 1996; Thomas and Robinson, 2005) is consistent with strong attenuation in laboratory granular materials at kHz frequencies (O'Donovan et al., 2016), but qualitatively differs from the slowly attenuating seismic reverberation model (Cintala et al., 1978; Cheng et al., 2002; Richardson et al., 2004, 2005), that is supported by measurements of slow seismic attenuation rates in lunar regolith (Dainty et al., 1974; Toksöz et al., 1974;

Nakamura, 1976). While both impact induced seismic 'jolt' and reverberation processes can cause crater erasure and rim degradation (Richardson et al., 2004, 2005; Thomas and Robinson, 2005; Asphaug, 2008), it is often assumed that size segregation induced by the Brazil nut effect depends on sustained vibrations or reverberation (e.g., Miyamoto et al. 2007; Tancredi et al. 2012; Matsumura et al. 2014; Tancredi et al. 2015; Perera et al. 2016; Maurel et al. 2017; Chujo et al. 2018). However, a series of strong taps, separated in time, can also bring larger particles to the surface (e.g., https://www.youtube.com/watch?v=XTM-okBCX8U).

Even cohesionless or low strength rubble would transmit an impact generated compression wave. However, asteroid rubble may have a low tensile strength of ~ 10 Pa (Sánchez and Scheeres, 2014; Scheeres and Sanchez, 2018). Impact generated seismic waves may not effectively rebound or reflect from asteroid surfaces. When they reach the surface, strong seismic waves can cause the surface to deform, induce landslides and loft particles off the surface (e.g., Tancredi et al. 2012), reducing the amplitude of reflected waves, increasing the attenuation rate and reducing the seismic reverberation time.

Simulations have shown that the Brazil nut effect is still effective in low gravity environments with $g \sim 10^{-4}$ (Tancredi et al., 2012; Chujo et al., 2018; Matsumura et al., 2014; Maurel et al., 2017). Simulations by Matsumura et al. show that the time for a particle to rise to the top of a granular mix is proportional to the square root of the gravitational acceleration of the body. The low gravity of asteroids will only affect the time scale of the granular flow due to the Brazil nut effect (Maurel et al., 2017). That is, size segregation due to the BNE is still effective in low gravity environments, it only takes longer for the process to proceed.

Shinbrot et al. (2017) proposed that pebbles accreting or falling onto the surface of an asteroid would tend to rebound from boulders, but sink into pebbly regions leading to lateral size segregation on a surface, a process they called 'ballistic sorting'. Since a pebble sea contains numerous pebbles, a particle landing there causes numerous collisions, making granular beds good impact absorbers due to their low coefficient of restitution (Meakin et al., 1986; Herrmann et al., 1997). Shinbrot et al. (2017) illustrated the effect with numerical simulations and by experimentally dropping glass beads and pebbles onto flat surfaces and surfaces containing mixtures of pebbles. They did not discuss the source or velocity distribution of the landing material.

Using numerical simulations, Tancredi et al. (2012) explored launching of ejecta from a surface in low gravity due to a subsurface seismic pulse traveling

3

through a granular medium. However, Tancredi et al. (2012) did not study the kinematics of the launched ejecta during landing and whether ejecta launched by impact excited seismic waves could leave boulders stranded on the surface.

Using laboratory experiments in a polydisperse granular medium, we explore surface modification due to ballistic sorting of the ejecta from an upward propagating subsurface pressure pulse that is strong enough to launch surface particles into the air. In section 2 we describe our experimental setup. With high speed video in section 2.2 we use particle image velocimetry to measure velocity vectors of ejecta particles. In section 3 we use scaling relations for seismic energy efficiency of an impact to estimate the importance of impact generated seismic pulses as a size segregation and surface modification process on rubble asteroids. A summary and discussion follows in section 4.

2. Laboratory experiments of upward propagating pressure pulses in a polydisperse granular medium

A bowl of granular polydisperse colored dry gravel is used to mimic the uppermost layer of a rubble pile asteroid. We hit the bottom of the gravel (not the bowl itself) with a strong impact and film the granular surface with high speed video as particles are launched into the air. An accelerometer in the bowl is used to characterize the pressure pulse strength and duration as a function of time. The experimental setup is illustrated in Figure 1.

Soft sphere granular models find that wave speed depend on pressure as this sets the strength of elastic contacts in force chains (Makse et al., 2004). With lower speeds near the surface, seismic waves would approach the surface at a near normal angle. To mimic this behavior we restrict our study to upward directed impacts into a granular media with an initially horizontal upper surface and in a container with a horizontal flat base. We have sifted the gravel to remove small particles (sand) and minimize the dissipative role of air flow. We recognize that the modest size of our experiments, the fact that we carry them out in air, not vacuum, and that our lab is not in milli or microgravity, may give us experimental results that are not representative of seismicity on a rubble pile asteroid.

The granular medium consists of materials commonly used in construction in Upstate NY. We use small and larger particles of crushed shale and medium sized particles of quartzite. Since our gravel is irregularly shaped all sizes were measured along their longest dimension. The smallest particles are 5 to 10

4

mm in length. The medium sized particles range in size from 15 to 25 mm and the largest particles from 30 to 55 mm. We mixed the gravel by hand. The mixture is predominantly the small particles, with about 20 medium sized particles, and up to five of the largest particles.

To minimize the role of air we sifted out powdered material and particles finer than about 5 mm. Experiments have shown that a fluid (e.g. air, water) present in a granular system can accelerate the ratcheting of a large particle compared to just convectively driven motion (Clement et al., 2010; Naylor et al., 2003). Möbius et al. (2005) showed that if the relative sizes of particles in the mix is small ($D/d < 10$) then air-driven size separation is negligible. They also found that air drag on the intruder was negligible and only the drag from the smaller particles contribute significantly. For the size distributions in our mix we find the relative size for the medium to small particles to be 2.5 - 3 and the relative size for the large to small particles to be 5.5 - 6. Therefore, the effects of air can be safely ignored in our experiments.

Gravel particles are painted with different fluorescent colors so we can see if particle velocities are dependent on particle size. The paint was applied from a spray can in a thin layer to not change the shape of the particles. We measured the angle of repose to be 34 degrees for both the bare and painted gravel mixture. Painting the rocks did not significantly change the friction between particles.

The experiment was lit with bright blue LEDs, causing the painted gravel to fluoresce. This allowed the tracking of different sized particles so we could see if ejecta velocities and particle trajectories were dependent on particle size. Smaller particles are painted fluorescent orange, though the un-dyed regions appear blue in our images because of our lighting. Medium sized particles are painted fluorescent green and the largest ones are painted fluorescent yellow. We were careful to use fluorescent paints that were detected as bright by our high speed camera, finding that our camera is insensitive to common red fluorescent paints and that different shades of blue paints were indistinguishable.

The gravel was held in a 25 cm diameter plastic bowl with a 5 cm diameter hole drilled in the bottom. A flat metal disk with a diameter of 8 cm was placed over the hole to spread the pulse over a wider area. The disk was not fastened to the bowl so free to move, and it is strong enough not to deform under the weight of the gravel or when it is struck by the lever arm. This contributed to the impactor's momentum going into accelerating the gravel, not the bowl. We covered the disk and the inside of the bowl loosely with

black cloth wrap to keep granular material from falling below the disk and through the hole. Since the disk was not held in place and loosely covered with a cloth air can still flow freely in the granular mix.

Our granular mixture filled the bowl to a depth of about 6 cm at the center. Five 1 kg weights are placed symmetrically on the bowl rim to reduce elastic vibrations in the bowl and reduce how far the bowl moves during the impacts. We painted a 1×0.5 cm scale bar on one of the wieghts in green fluorescent paint. We use this scale bar to derive the pixel scale used to track particle velocities and motions between frames. More details on particle tracking are given in section 2.2.

A weight up to one kilogram was dropped from a height of 15 cm onto a metal plate at the back of the lever arm. The arm then rotates and the hammer end strikes the metal disk inside the bowl. The levered hammer provided repeatable single pulses. The hammer stays in contact with the metal disk until the weight is manually removed from the plate. The pressure pulse travels through the granular media upward and emerges on the top surface as a radial wavefront where it lofts gravel into the air. After each impact the gravel is remixed as specified above.

We filmed the ejecta from the side with a Chronos 1.4 high speed camera at 1057 frames per second and from above at 30 frames per second with a Nikon V1 for all experiments. An accelerometer was buried in the gravel about 3 cm below the surface, allowed us to record acceleration as a function of time in the gravel. Figure 8 shows the accelerometer data for each experiment listed in Table 1. The Arduino Mega was programmed to record data when the accelerometer readings exceeded about 8g. This threshold is given by the dashed black line in theses figures. Experiments are labelled consecutively by number in our lab notebooks. The experiments discussed in this paper are denoted with numbers 39, 41, 42 and 43.

Only four experiments are shown in this paper because these were the best quality complete data sets. A complete data set included high quality high-speed (1057fps) and normal speed (60fps) videos, and accelerometer measurements. High quality videos were considered those that had the ejecta curtain entirely in focus and in frame, good lighting so that the ejecta curtain would not cast a shadow on itself. Quality accelerometer data did not include clipping in the data from the accelerometer being too slow to capture it. An experiment's data set was considered incomplete if the quality of the videos or accelerometer did not meet requirements, or if the cameras or accelerometer were not triggered resulting in no data. We observed ballistic sorting upon

6

Table 1: Impact Experiments

Experiment #	Peak Acceleration	Pulse Duration
39	12 g	10 ms
41	18.5 g	10 ms
42	50 g	3 ms
43	37 g	3 ms

Notes: The experimental setup is shown in Fig. 1. Peak acceleration are the maximum seen in the acceleration profiles (see Figure 8). Pulse durations were measured from the full duration at half maximum of the acceleration profile.

material landing for all experiments performed regardless of data acquired.

An impact can be described with a maximum acceleration value and a pulse duration. We can adjust the pressure pulse amplitude, by dropping a heavier weight or increasing its initial height. We adjust the pulse duration by inserting or removing a piece of foam between the impactor and plate. We see broader pulses with thicker foam.

2.1. Boulder stranding with a single impulse

During each impact experiment we take two simultaneous videos, one from above (shown in Figure 2) and one from the side (shown in Figures 4 - 7). Thumbnails (and links) for the eight videos are shown in Figure ??. Simultaneously we measure acceleration as a function of time with the accelerometer (accelerometer profiles are shown in Figure 8). The pulse duration was measured by taking the full duration at half maximum of the acceleration profile. The impact experiments we discuss are listed in Table 1. In the table, we list peak acceleration values in units of g, the gravitational acceleration on Earth, and the pulse duration in milliseconds measured from the accelerometer profiles.

The pulse was measured using an ADXL377 chip 200g accelerometer and recorded using the analog to digital converter of an Arduino Mega. We found that the acceleration profiles in time are not strongly dependent upon the depth that the accelerometer was buried, unless it was touching the base plate or surface. Figure 8 shows the pulse profiles (acceleration as a function of time) recorded for each experiment. Pulses for experiments 39 and 41 had amplitudes less than 20g and a duration of 10ms. Experiments 42 and 43 had pulses with amplitudes greater than 30g and duration of 3ms. The time for
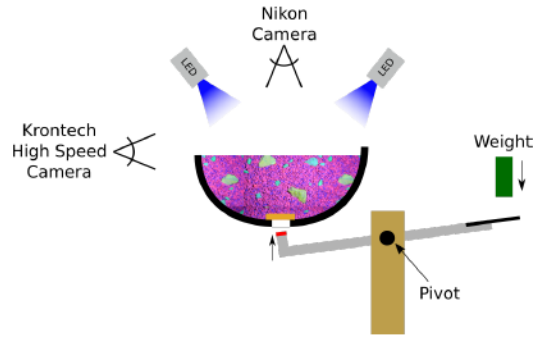
Figure 1: Illustration of our experimental setup for filming particles launched into the air by a subsurface pulse. A lever arm (gray bar) rotates on a pivot when a weight is dropped onto a metal plate (black line at end of lever). A metal piece attached to the lever rotates up and hits a metal disk inside the bowl of gravel (orange rectangle at bottom of bowl). The bowl's motion is reduced by adding weights to the rim (not shown). Two blue LEDs are used to light gravel particles that are painted with pink, green, and yellow fluorescent paints. The largest particles are painted yellow, medium sized particles are green, and smallest particles are in pink. The gravel illustrated in the bowl is not to scale. A Nikon camera was positioned above the bowl to film the ejecta from above. A Krontech high speed camera was positioned at the side of the bowl and at a height approximately level with the surface of the gravel. For all experiments the gravel had a depth of 6 cm at the center. The lever arm allowed us to carry out experiments with similar pulse amplitudes. The pulse amplitude was varied by changing the mass of the dropped weight or its initial height. The pulse duration was adjusted by adding or removing a small piece of foam to the tip of the impactor (shown as a red square at the tip of impactor).
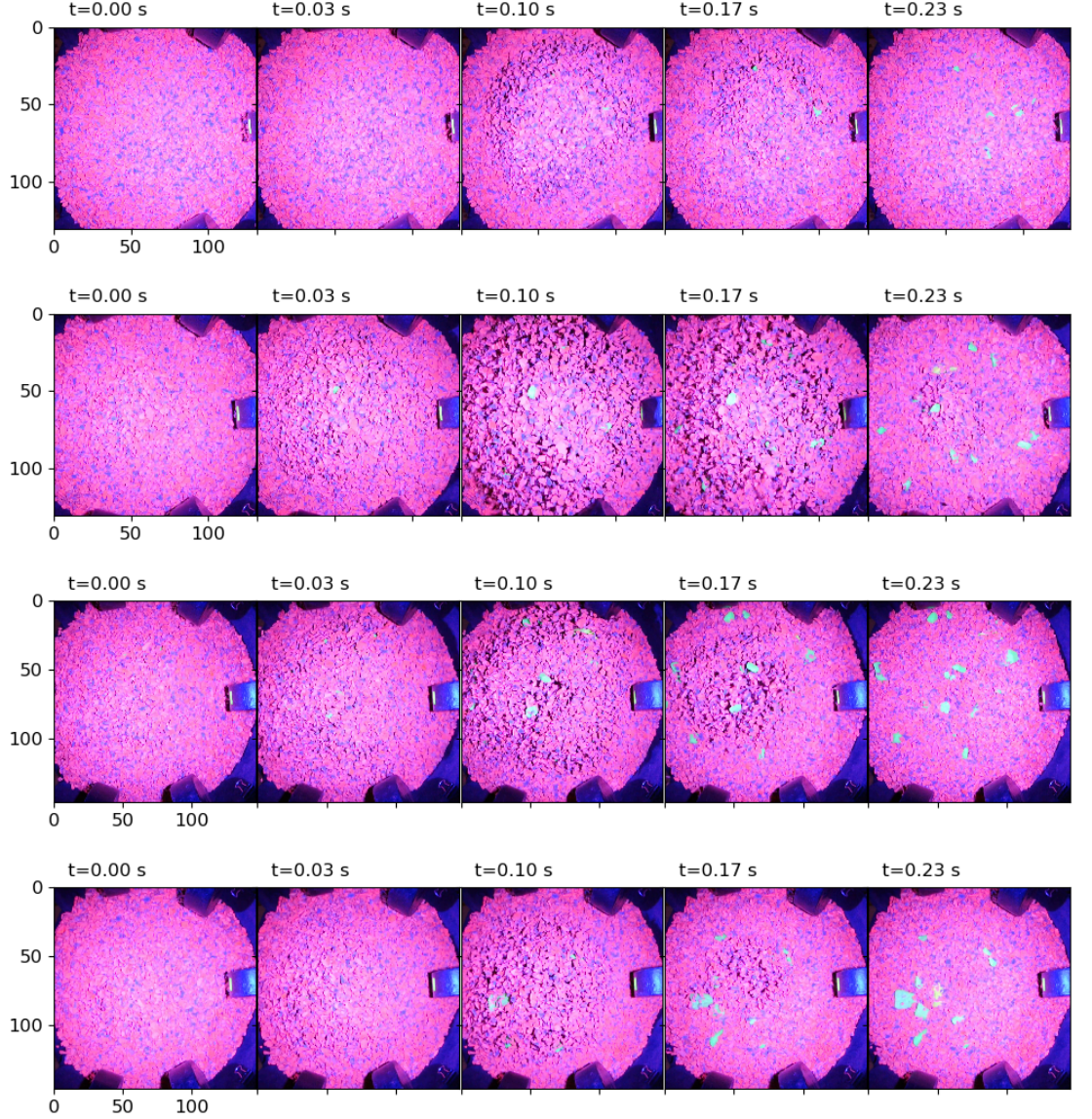
Figure 2: Frames from regular speed video viewing the granular surface from above and looking directly downward. The top two rows show the weaker pulse (39 and 41 respectively) impact experiments and the two bottom rows show the stronger pulse impact experiments (42 and 43 respectively). These experiments are listed in Table 1. The x and y axes for leftmost panels give the scale in mm. We measure time from when surface particles start to move upward. The time of each image is listed on top of each frame. Particles are painted with fluorescent paints and are lit with blue LEDs. Larger particles are painted green and yellow and smaller particles are painted pink. Some sides of the smaller particles are not covered in paint and appear blue due to the lighting. Frames on the right show that larger particles are lofted due to the subsurface impulse and left stranded on the surface afterwards. Previously buried boulders are stranded on the surface in all our experiments.

sound waves to travel across the depth of the bowl (0.6 ms if at a speed 100 m/s across 6 cm) is less than the durations of our pulses, so these durations give the durations of bulk material motions in the bowl.

Figure 2 shows images taken from the 30 frames per second video looking down on the surface at different times for the four impact experiments listed in Table 1. From top to bottom, each panel corresponds to experiments 39, 41, 42, 43 respectively. We measure time from when the surface starts to move. In all impact experiments, we see large particles, seen as green or yellow in the images, are buried prior to impact and are on the surface after impact. The large particles initially have random depths but we checked that large particles were not initially shallower than 0.5 cm below the surface. It is clear from the figures that regardless of different pulse amplitudes and durations, large particles are stranded on the surface after a single impact. The particles on the surface after impact are also seen in the high speed videos that are included in the supplemental material. The experiments are robust and repeatable. The experiments show that a series of pulses, continuous vibration, or reverberation is not necessary to bring initially buried large particles to the surface.

We found that pulses with larger peak accelerations are able to excavate deeper boulders. Large particles that are already on the surface tend to stay there after a second or third impact. Pulses that are too weak (less than 10 g) and short (less than a few ms) were ineffective at stranding larger particles on the surface. All the experiments shown here launched particles into the air, so they all have pulses with accelerations above surface gravity. The ejecta travel upward a few cm and so travel a vertical distance that is greater than the stranded large particle heights. The impacts cause all the material in the bowl to move upwards, so the depth of launched material also exceeds the large particle lengths. We will use these conditions when we discuss regimes for boulder stranding in section 3.

2.2. Particle tracking

We use the soft-matter particle tracking software package `trackpy` (Allan et al., 2016) to identify and track gravel particles in the video frames. `Trackpy` is a software package for finding blob-like features in video, tracking them through time, and analyzing their trajectories. It implements and extends the widely-used Crocker-Grier algorithm (Crocker and Grier, 1996) in Python.

We measure velocity vectors at six different times in the high speed videos and for our four impact experiments. At each start time we extract 20 consecutive frames and track particles in them, constructing about 1000 particle trajectories. The particle velocities are computed from particle positions over four frames or 3.78 ms apart. The velocity vectors are shown along with images from the high speed videos in Figures 4-7 for the four impacts. As before, times are labeled on the top of each image panel with time measured from when surface particles start to move upward.

In all four experiments, Figures 4-7 show that at early times the particles are moving upward as particles leave the surface. Ejected particles move together. During the time the gravel is launched until just before landing, nearby particles have similar velocity vectors. The last panels in Figures 4-7 show that as particles land the velocity vectors are randomly oriented, implying that scattering is taking place.

While they are in the air, larger green particles have similar velocities to smaller red particles that in are proximity. Figure 3 shows the standard deviation of the difference in the angles of the velocity vectors of the green and red particles as a function of the distance between one green particle and a red particle. The angles of the red particles' velocity vectors are subtracted from the angle of one green particle in the ejecta curtain. This angular difference is found for all red particles within some distance from the green particle. The standard deviation of the angular difference is then found and plotted as a function of this distance. The blue circles show the standard deviation calculated for the ejecta at a time when the curtain reached near max height and the orange diamonds at a time when the material is landing. Both times used the same green particle. For earlier times, when the ejecta is moving upward, the standard deviation of the difference in velocity directions is small for nearby particles and increases as more distant particles are included. Later in time the standard deviation is large for nearby particles and varies with increasing distance. This shows that red particles in close proximity to the green particle are moving together with similar velocities early in time and are scattering later in time.

We find that the ejecta velocities and trajectories are independent of particle size, as is true for crater ejecta (Hirata and Nakamura, 2006). Thus the tendency for large particles to be on top after particles land must be due to scattering that happens upon landing. We infer that the ballistic sorting process (Shinbrot et al., 2017) is the reason that larger particles remain uncovered after all the ejecta has landed.

The fastest ejected particles are in the center of the bowl and directly above the impact site. Particles that are more distant from the center land earlier than particles launched from the center of the bowl. We suspect that particles originally below the surface are ejected with somewhat lower velocities than particles that are originally on or near the surface, as observed in the simulations by Tancredi et al. (2012), though it is difficult to track these lower particles as they are obscured by particles that leave the surface earlier. The particles underneath that are launched later into the air, land earlier. Particles launched into the air earlier scatter of the lower particles as the ejecta lands. We do not see faster particles overtaking and scattering with slower particles in the air, suggesting that the magnitude of the velocities are similar.

To check that the pulse acceleration profiles are consistent with the velocity of ejected particles, we estimate the velocity of the pulse by taking the max acceleration and multiplying by the pulse duration. In this way, we calculate ejecta velocities of about 1.2, 1.2, 1.5, and 1.1 m/s for experiments 39, 41, 42, and 43 respectively. Velocities measured in our experiments were lower by a factor of two from what was estimated. When the profile is integrated over the total time of the experiment, the ejecta velocities are approximately consistent with the velocities estimated from the acceleration profiles. This implies that the acceleration profiles are consistent with the observed particle trajectories.

The ejecta pattern due to a subsurface seismic pulse differs remarkably from that of an impact crater. An impact crater ejecta during a snapshot is in the shape of a cone because there is a relation between ejecta time, velocity and angle. This means that few particles are in proximity when they land. For a seismic pulse, nearby particles are launched a similar times and with similar velocities and so land in proximity. Thus we expect more particle-particle collisions in ejecta caused by seismic pulses than in crater ejecta. Crater ejecta would scatter with particles already present on the surface, but would be less likely to scatter with each other. A boulder present on the surface could remain there, but only a boulder that is launched in the crater ejecta could become stranded on the surface. In contrast, ejecta launched by a seismic pulse and containing boulders would suffer collisions between ejecta particles as well as surface particles upon landing.

We estimate the coefficient of restitution from the ratio of particle's speed after they scatter (on landing) to their descent speed just prior to scattering. The approximate ratios of the vectors lengths in Figures 4-6 (taking the

ratio of the vector lengths for a few particles) is about 1/3. The coefficient of restitution is relevant for momentum exchange during particle-particle collisions. Every collision reduces the relative normal speed by the restitution coefficient. If the coefficient of restitution is very low then small particles would stop moving after scattering and they would only leave a larger particle uncovered if they were perched unstably on it after landing. With a larger coefficient of restitution a small particle can be scattered far enough away to leave a larger particle uncovered, though the distance travelled should exceed the width of the larger particle.

The pulse, as it travels through the medium, loses energy and spreads out due to particle-particle contacts and friction. Ejection velocities are greatest at the center of the ejecta plume and decrease further away from the center. The initial velocity vectors are not vertical away from the center. This means that particles are on diverging trajectories and particles tend to move or be scattered away from the center, making it possible to strand a larger particle in the center of the bowl than near the rim. This implies that the shape of the seismic waves in our experiments are spherical. Pulse propagation through an asteroid may be inconsistent due to interior properties changing the pulse shape. However, so long as the pulse is strong enough to accelerate material off of the surface then some of the phenomena seen here might also arise on them.

We also found that once a large particle is stranded it tends to stay there and not be reburied. The number of large particles stranded on the surface was dependent on its depth. A single pulse can excavate a boulder if the acceleration of the seismic pulse is greater than the surface gravity (no material is ejected), vertical distance of the ejected material is greater than the boulder height (ejected material is above the large boulder and thus can scatter on landing), and the depth of material ejected is larger than the boulder height (otherwise boulder stays buried). We use these three conditions in Section 3 to predict a regime for boulder stranding.

When multiple pulses, separated in time, are sent through the gravel mix we found that they continue to excavate large particles. Once the particles are on the surface they tend to remain there after multiple pulses. Due to the absence of material above the large particle in the ejecta curtain nothing is present to bury the boulder upon landing. If the acceleration of the pulse is below the surface gravity then no material is lofted into the air, but size sorting is still observed. In this case, the BNE is driven by a ratcheting effect versus a ballistically sorted BNE.
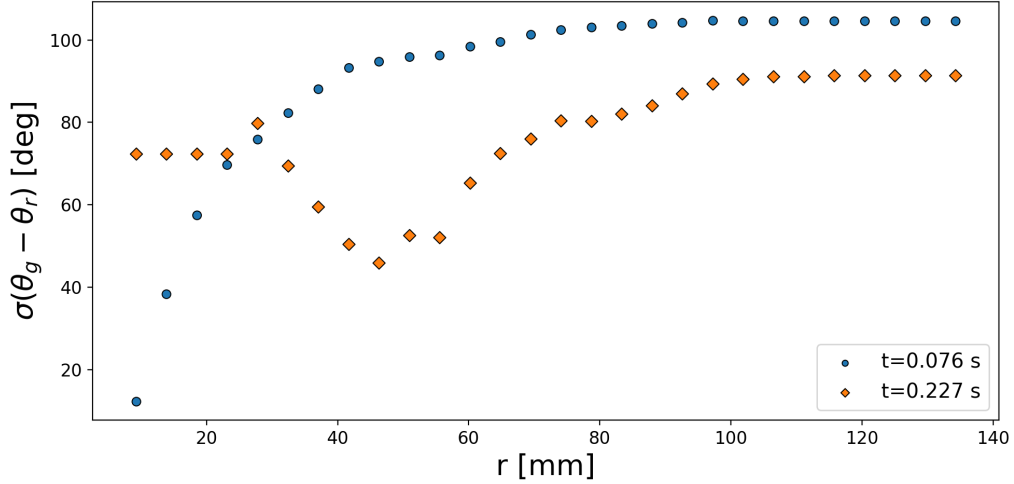
Figure 3: Plot of the standard deviation of the difference in the angles of the velocity vectors of the green and red particles as a function of the distance between a green particle and a red particle. The angles of all the red particles' velocity vectors within a distance r are subtracted from the angle of one green particle in the ejecta curtain. The blue circles show the standard deviation calculated for the ejecta at a time when the curtain reached near max height and the orange diamonds at a time when the material is landing. Both times used the same green particle. For earlier times, when the ejecta is moving upward, the standard deviation of the difference in velocity directions is small for nearby particles and increases as more distant particles are included. Later in time the standard deviation is large for nearby particles and varies with increasing distance. This shows that red particles in close proximity to the green particle are moving together with similar velocities early in time and are scattering later in time.

In summary, our laboratory experiments illustrate that a single subsurface pressure pulse that lofts surface material can leave previously buried large particles on the surface. The mechanism is robust as every experiment we ran showed the phenomenon. Particle trajectories show that nearby particles have similar velocity vectors while particles are in the air but are randomly oriented upon landing when they scatter. Nearby but different sized particles also exhibited similar trajectories while in the air, implying that larger particles were left on the surface because of collisions that took place upon landing.
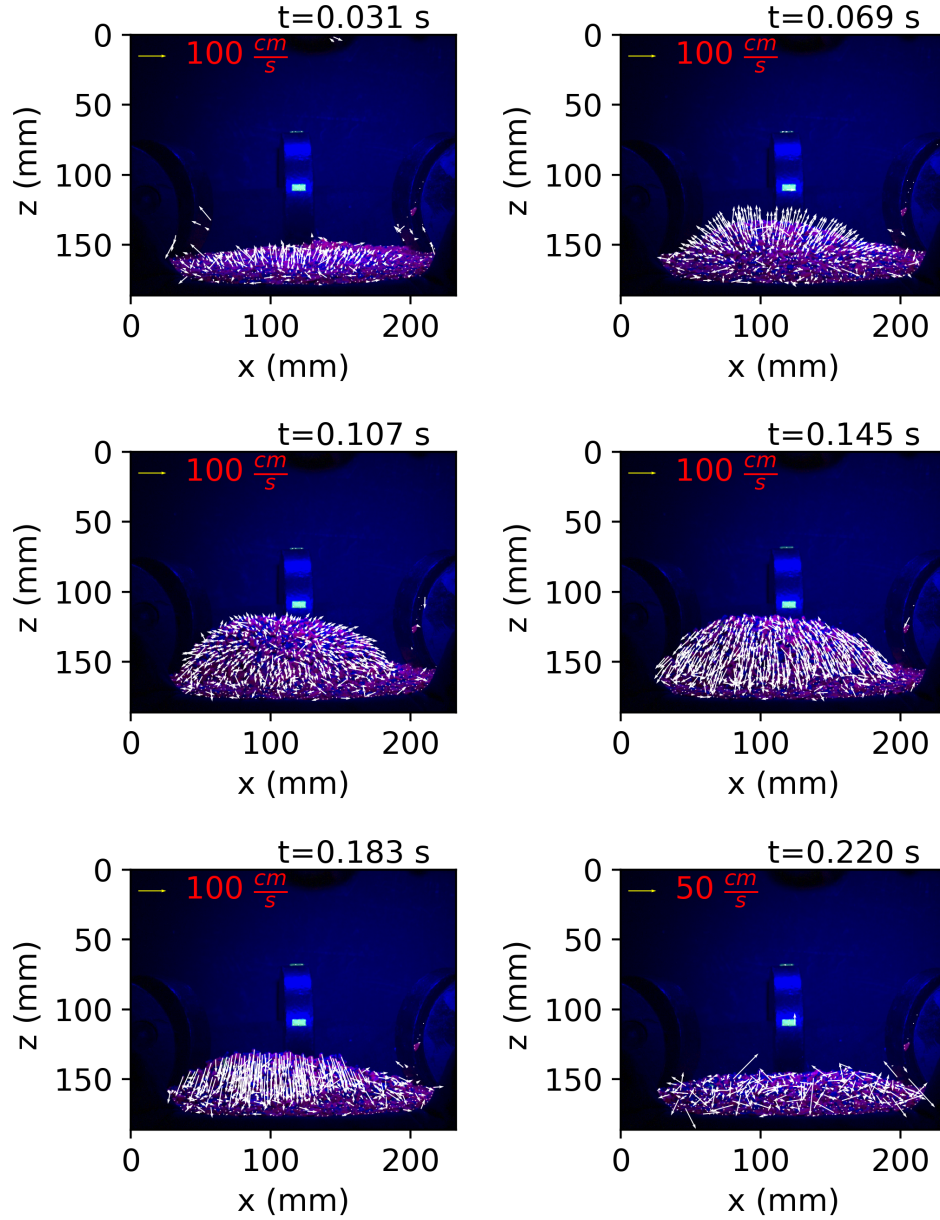
14

Figure 4: Snapshots from the high speed video (1057 frames per second) of experiment 39 overlaid with velocity vectors of individual particles. The time of each panel is shown on the top of the panel and is measured from when particles start to move upward. The yellow arrows in the top left corner show the scale of the velocity vectors in cm/s. Nearby particles tend to have similar velocity vectors throughout trajectory, except during landing when significant scattering occurs. The blue rectangle in the background is a weight used to keep the bowl down. On it, there is a green 1×0.5 cm scale bar.
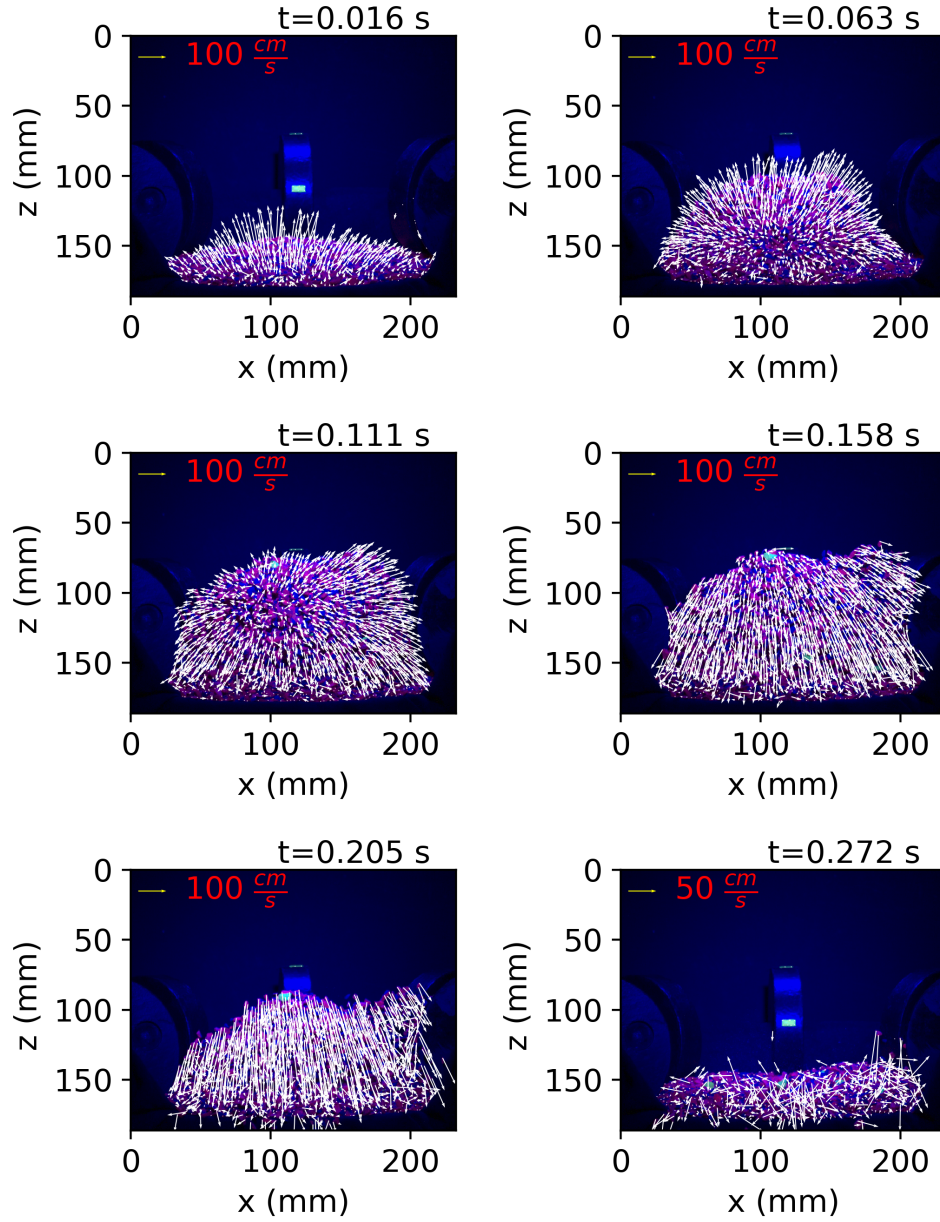
15

Figure 5: High speed video snapshots of experiment 41 and similar to Figure 4. Snapshots show similar features as in Figure 4. A large green particle in the middle panels has similar velocity vectors to nearby smaller particles. We see no evidence that larger particles have different velocity vectors than smaller particles prior to landing.
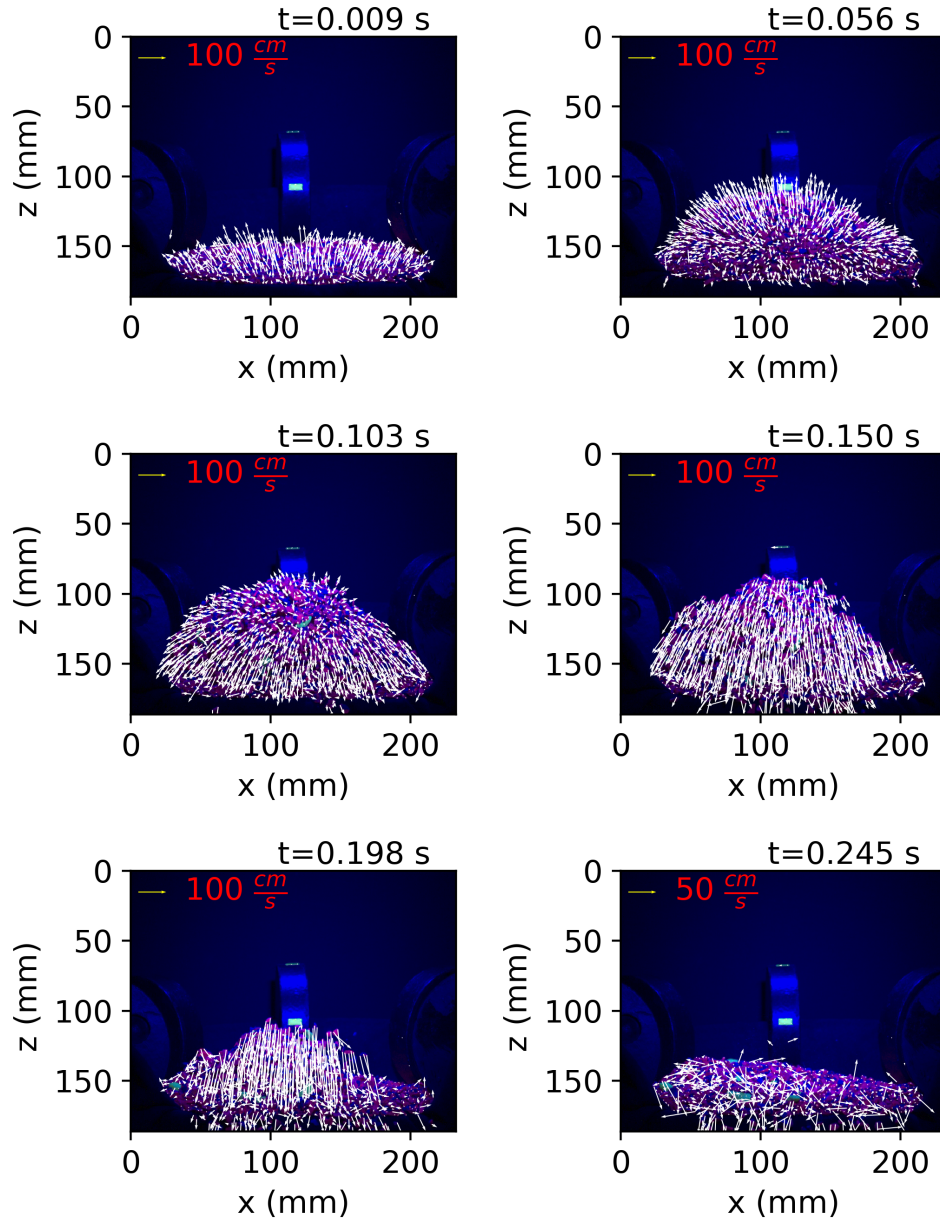
16

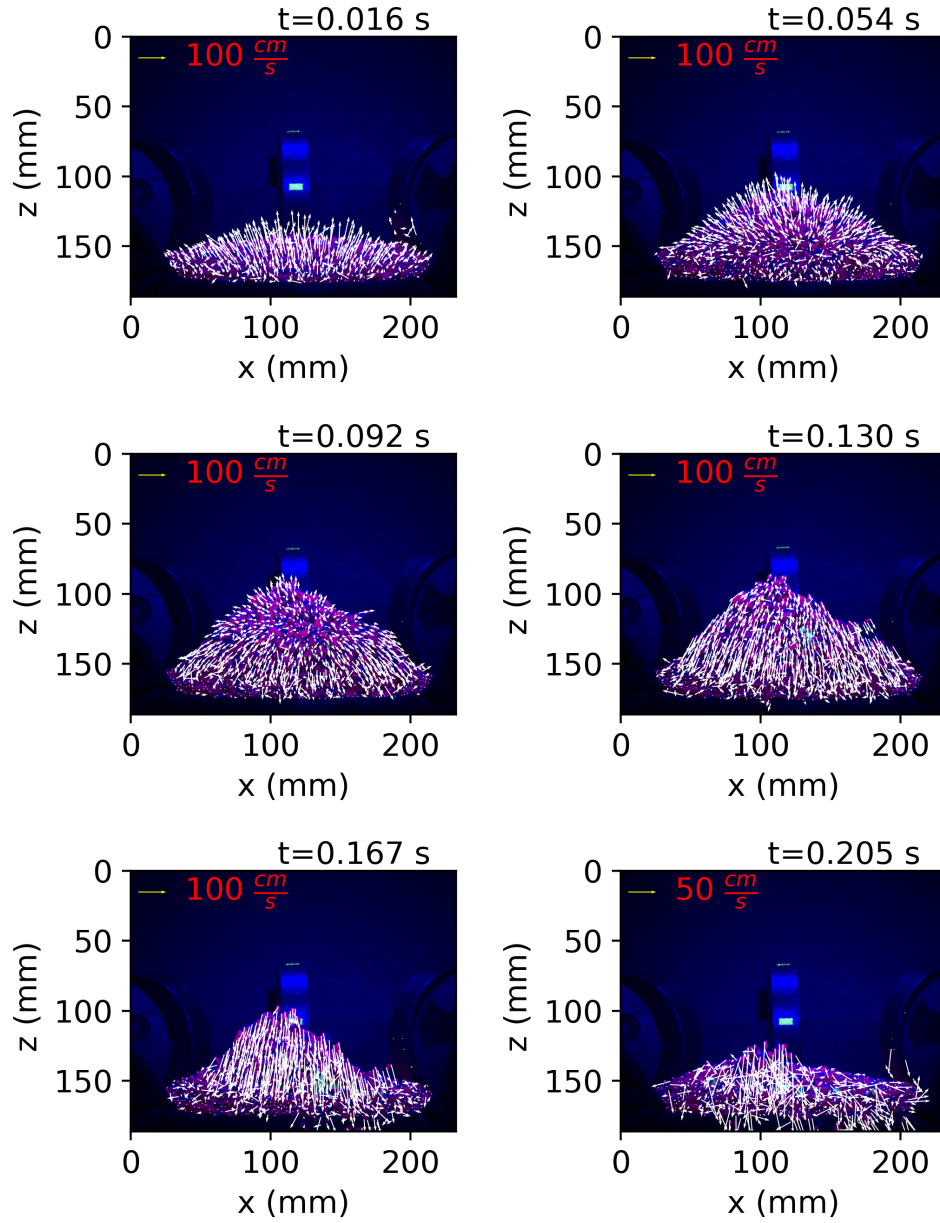Figure 6: High speed video snapshots of experiment 42 and similar to Figure 4.

Figure 7: High speed video snapshots of experiment 43 and similar to Figure 4.

Table 2: Nomenclature

Mass of asteroid	M
Radius of asteroid	R
Density of asteroid	ρ
Surface gravitational velocity	$V_{\mathrm{grav}} = \sqrt{GM/R}$
Surface gravitational acceleration	$g = GM/R^2$
Diameter of asteroid	D
Diameter of projectile	D_{proj}
Mass of projectile	m_{proj}
Velocity of projectile	V_{proj}
Kinetic energy of projectile	$E_{\mathrm{proj}} = \frac{1}{2}m_{\mathrm{proj}}V_{\mathrm{proj}}^2$
Total radiated seismic energy	E_s
Seismic efficiency	$\epsilon_s = E_s/E_{\mathrm{proj}}$
Diameter of crater	D_{crater}
P-wave speed	V_p
Seismic source duration	τ_s
Peak seismic frequency	$f_s \sim 1/\tau_s$
Exponent for impact scaling	μ
Depth of ejected material	h_{ejected}
Maximum height reached by ejecta	h_{max}
Boulder height	h_{boulder}
Distance from impact site	d
Travel attenuation function	$f_{\mathrm{travel}}(d)$
Amplitude of velocity displacement in pulse	$v_u(d)$
Amplitude of velocity displacement in pulse near crater	A_u
Source time parameter	X_s

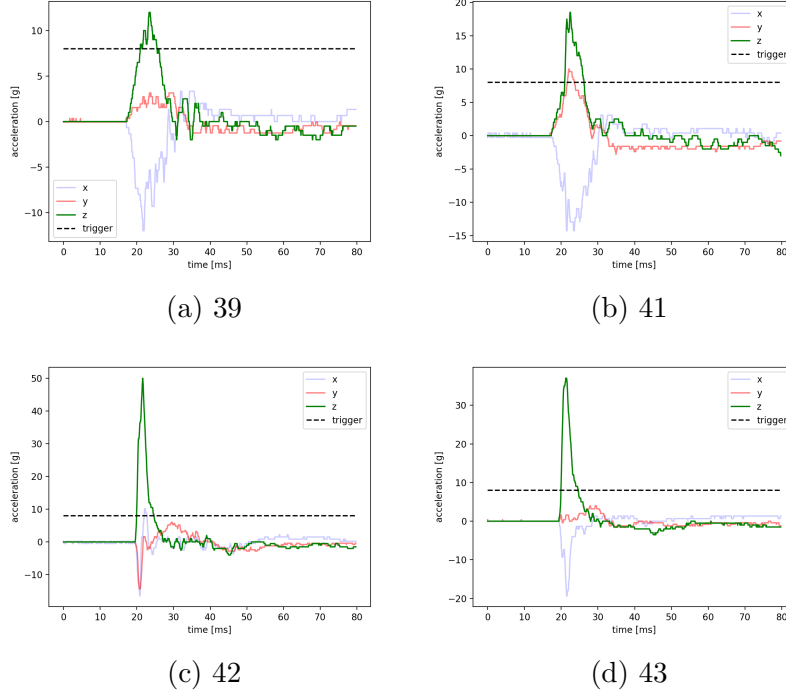(a) 39   (b) 41

(c) 42   (d) 43

Figure 8: Accelerometer measurements of subsurface pulse. Data was measured using an ADXL377 200g accelerometer buried 6 cm below the surface of the granular mixture and connected to an Arduino Mega. Weaker pulses ($> 20g$) are shown in a) and b) and stronger pulses ($< 30g$) are shown in c) and d). The accelerometer was positioned in the bowl so that the z-axis is in the vertical direction and the x and y axes are in a plane parallel to the surface of the granular mixture.

3. Regime for Boulder stranding via an impact excited seismic pulse

In the previous section we presented laboratory experiments showing that larger particles that are previously buried can emerge on the surface following a single upward propagating subsurface pressure pulse that lofts particles into the air. In this section we consider the possibility that a seismic pulse excited from an energetic impact can cause boulders to be stranded on rubble pile asteroids such as 162173 Ryugu, 101955 Bennu and 25143 Itokawa. We assume that both the asteroid and impactor are spherical and the collision is head-on. Nomenclature used in this section is listed in Table 2.

We describe the excitation of a seismic pulse from a meteoroid impact

20

in terms of two parameters, the seismic efficiency, ϵ_s, and the seismic source time τ_s. As these parameters are poorly constrained, instead of assuming approximate values for them, we search for a regime that allows boulders to be stranded on the surface. We estimate the amplitude A_u of the velocity of displacement motions in the seismic pulse. To correct for travel distance and spreading of energy , we assume that the pulse amplitude

$$v_u(d) = A_u f_{\text{travel}} \left(\frac{D_{\text{crater}}}{d} \right) \tag{1}$$

depends on a function f_{travel} of the distance traveled d, but we neglect dispersion and so do not vary the pulse duration τ_s. Simulations by Tancredi et al. (2012) find that particles ejected from the surface by a pressure pulse have ejection velocities similar to $v_{\text{eject}} \sim v_u$, the displacement velocity amplitude in the pulse. We estimate the depth of lofted material h_{eject} from the ejection velocity and the kinetic energy per unit area in the seismic pulse. Our experiments suggest that a boulder can be stranded on the surface if

- Accelerations in seismic pulse excited by the impact are above that of surface gravity.

- The vertical distance traveled h_{max} by material lofted above the surface is greater than the boulder height, h_{boulder}.

- The depth of material lofted h_{eject} is larger than the boulder height.

The kinetic energy of the projectile $E_{\text{proj}} = \frac{1}{2}m_{\text{proj}}V_{\text{proj}}^2$ with mass m_{proj} and velocity V_{proj} can be compared to the total radiated seismic energy, E_s, giving a seismic efficiency factor

$$\epsilon_s \equiv \frac{E_s}{E_{\text{proj}}}. \tag{2}$$

Estimates for the seismic efficiency range from $\epsilon_s \sim 10^{-2}$ to 10^{-6} (see experiments, simulations and discussions by McGarr et al. 1969; Schultz and Gault 1975; Melosh 1989; Richardson et al. 2005; Shishkin 2007; Lognonné et al. 2009; Yasui et al. 2015; Güldemeister and Wünnemann 2017).

For a pressure pulse with half width (in time) τ_s, the width in space of the traveling seismic pulse is $\sim V_p \tau_s$ where V_p is the p-wave speed. The total energy per unit volume in the seismic pulse emitted at the crater base is

proportional to ρA_u^2. The volume of displaced material is given by the area of the crater, $\pi D_{\text{crater}}^2/4$, times the spatial width of the pulse. The seismic energy is therefore given by

$$E_s \sim \rho A_u^2 \frac{\pi D_{\text{crater}}^2}{4} V_p \tau_s. \tag{3}$$

Using the seismic efficiency and projectile mass and velocity, the amplitude in displacement velocity of the seismic pulse as it leaves the crater base

$$A_u^2 \sim V_{\text{proj}}^2 \frac{\epsilon_s}{3} \frac{D_{\text{proj}}}{V_p \tau_s} \left(\frac{D_{\text{proj}}}{D_{\text{crater}}} \right)^2 \tag{4}$$

and we have assumed similar densities for asteroid and projectile; $\rho_{\text{proj}} \sim \rho$. A particle ejected from the surface at velocity $v_{\text{eject}} = v_u$ at distance d from the impact site would reach a maximum height of travel

$$h_{\text{max}}(d) \sim \frac{v_u^2}{2g} = \frac{R A_u^2}{2 V_{\text{grav}}^2} f_{\text{travel}}^2(d) \tag{5}$$

where g is the gravitational acceleration at the surface.

In an elastic regime the function describing the decay of the seismic pulse amplitude $f_{\text{travel}}(d) \propto d^{-1}$ depends on the distance propagated. Scaling from the crater diameter and setting $d = D$, the asteroid diameter, for a pulse reaching the impact site's antipode, we assume $f_{\text{travel}}(D) \sim D_{\text{crater}}/D$. Inserting this into equation 5 and using equation 4, we estimate the ejecta reaches a vertical height above initial position

$$\left(\frac{h_{\text{max}}}{R} \right) \Big|_{d=D} = \frac{\epsilon_s}{6} \left(\frac{D_{\text{proj}}}{V_p \tau_s} \right) \left(\frac{V_{\text{proj}}}{V_{\text{grav}}} \right)^2 \left(\frac{D_{\text{proj}}}{D} \right)^2. \tag{6}$$

We can invert this equation giving a projectile diameter

$$(D_{\text{proj,hmax}}) \big|_{d=D} \sim D \left(\frac{6}{\epsilon_s} \frac{h_{\text{max}}}{R} \frac{V_p \tau_s}{D_{\text{proj}}} \right)^{\frac{1}{2}} \left(\frac{V_{\text{grav}}}{V_{\text{proj}}} \right) \tag{7}$$

in terms of the ejecta height. Equation 7 gives an estimate for a projectile that could strand a boulder on the impact site's antipode.

The velocity at which material is ejected from the surface should be similar to the displacement velocity of the seismic pulse

$$v_{\text{eject}} \sim v_u \tag{8}$$

22

Tancredi et al. (2012) in section 5 simulated the maximum height of ejecta from a sub-surface pulse. Using equation 5 and the velocity of our pulses we calculate max heights of 7, 7.5, 11, and 6 cm for experiments 39, 41, 42, and 43 respectively. These max heights have a similar order as given in Figure 15 of Tancredi et al. 2012 supporting that the ejection velocity is similar to the displacement velocity of the pulse.

The kinetic energy per unit area of ejected material is given by

$$e_{\text{ejected}} \sim \frac{1}{2} h_{\text{ejected}} \rho v_u^2. \tag{9}$$

The kinetic energy per unit area in the seismic pulse can be estimated by integrating over the pulse at a moment before it reaches the surface, $e_{\text{pulse}} \sim \int dx \, \rho v_u^2$. Assuming that the pulse travels with velocity V_p and that it's width has not spread in time (i.e. the pulse maintains it's shape),

$$e_{\text{pulse}} \sim \rho v_u^2 V_p \tau_s. \tag{10}$$

Equating these two estimates for kinetic energy gives us an estimate for the depth of ejected material

$$h_{\text{ejected}} \sim 2 V_p \tau_s. \tag{11}$$

The contact-and-compression phase of an impact excites a hemispherical shock wave in the ground that propagates away from the impact site (Melosh, 1989). As the shock wave propagates, it degrades into a purely elastic (seismic) wave. The structure of the elastic wave is expected to be complex, with multiple pulses associated with the elastic precursor to the shock wave, an elastic remnant to a plastic wave during the transition between shock and elastic wave, and reverberations associated with different seismic impedances in the target, rock fractures and compactification (see section 5.2.6 by Melosh 1989). Low velocity laboratory impacts into granular media measure source times (as a half width) of about 10 μs (Yasui et al., 2015). Similar durations are measured in sandstone targets (Hoerth et al., 2014) and are predicted via numerical simulation (Güldemeister and Wünnemann, 2017). These pulse durations may be shorter than excited by astronomical impacts, as the seismic source time τ_s could be longer for more energetic impacts (e.g., Lognonné et al. 2009). Missile impacts estimate peak seismic frequencies in the range $f_s \sim$ 10–40 Hz (Latham et al., 1970) and hydrodynamics simulations of asteroid impacts estimate a similar range (Richardson et al., 2005). We relate source time to frequency with $\tau_s \sim 1/f_s$.

To help identify the regime that allows boulders to be stranded we tentatively adopt a linear scaling between projectile radius and seismic source time, defining a parameter

$$X_s \equiv \frac{V_p \tau_s}{D_{\text{proj}}} \qquad (12)$$

similar to equation 5 by Lognonné et al. (2009) that is based upon calculations of seismic power radiated into a homogeneous elastic half-space (Wolf, 1944; McGarr et al., 1969). Setting seismic source time parameter X_s and requiring that $h_{\text{boulder}} > h_{\text{ejected}}$, equation 11 limits the projectile radius

$$D_{\text{proj,heject}} \gtrsim \frac{D}{4X_s} \frac{h_{\text{boulder}}}{R}. \qquad (13)$$

With $h_{\text{max}} > h_{\text{boulder}}$ and our definition for source time parameter X_s, we rewrite equation 7

$$(D_{\text{proj,hmax}})\,|_{d=D} \gtrsim D \left(\frac{6}{\epsilon_s} \frac{h_{\text{boulder}}}{R} \right)^{\frac{1}{2}} X_s^{\frac{1}{2}} \left(\frac{V_{\text{grav}}}{V_{\text{proj}}} \right), \qquad (14)$$

giving an estimate for the size of projectile that could strand a boulder on the impact site's antipode. A comparison between equation 13 and 14 shows there is a balance involving the seismic source time. If the source time is short, then little material is ejected, but ejected material reaches a larger height. If the source time is long, then more surface material is lofted, but not very high above the surface.

Equation 13 gives a projectile diameter capable of causing a boulder at depth h_{boulder} be ejected from the surface. Equation 14 gives the diameter of a projectile capable of causing ejecta to reach a height of h_{boulder}. For a boulder of height h_{boulder} to be stranded on the surface we assume that both conditions must be satisfied.

In Figure 9 we plot the projectile diameter as a function of asteroid diameter that would strand a boulder on the surface from a seismic pulse that ejects surface particles. Orange dashed and blue dot-dashed lines show equation 14 computed with $h_{\text{boulder}}/R = 0.01$ and 0.001, respectively. Orange and blue dots show equation 13 computed with the same ratios. Above the orange dots, the depth of ejecta $h_{\text{ejected}} > 0.01R$. Above the orange dashed line, the ejecta reaches a height $h_{\text{max}} > 0.01R$. Above dotted and dashed orange lines, shaded in darker orange, boulders with height $h_{\text{boulder}} > 0.01R$ could be stranded on the surface by a seismic pulse. Above dotted and dot-dashed
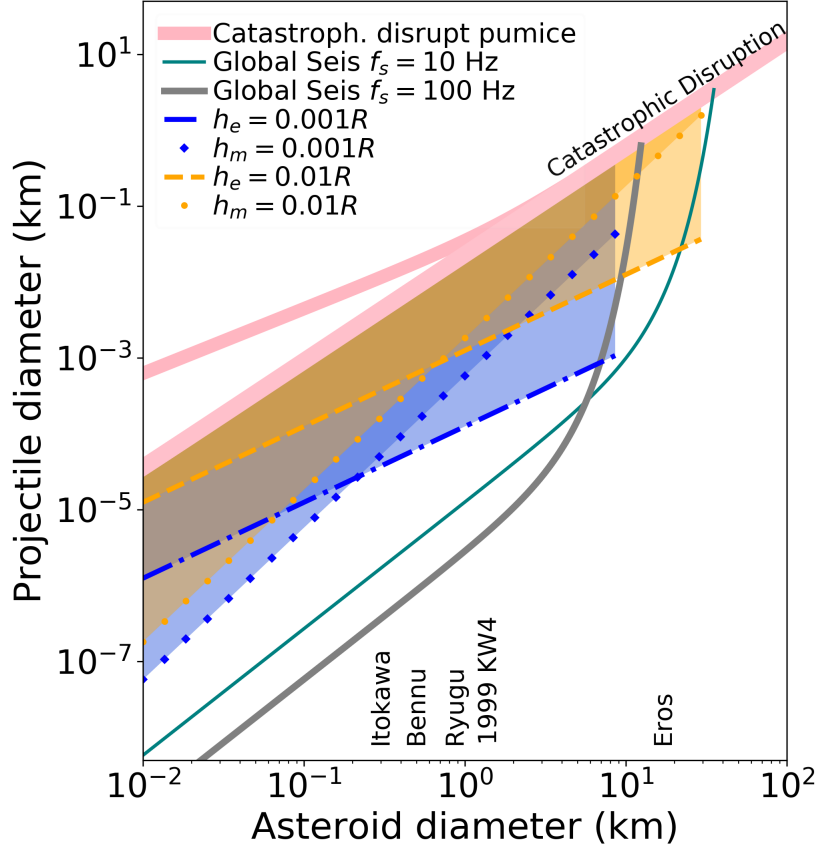
Figure 9: Scaling for impacts on asteroids. We show diameters of projectiles capable of catastrophic disruption (wide pink lines), global seismic shaking (green and grey solid lines) and for stranding boulders (orange and blue lines, dots and shaded regions). Above the dashed orange line, impacts cause seismic pulse ejected material to reach a height $h_{\max} > 0.01R$, where R is the radius of the asteroid. Above the orange dotted line, the depth of ejecta $h_{\mathrm{ejected}} > 0.01R$. We shade in orange the region above these lines and the catastrophic disruption line. The darker orange region is above both dotted and dashed orange lines, and is where boulders with height $h_{\mathrm{boulder}} > 0.01R$ could be stranded on the surface by a single seismic pulse. The dashed orange and dot dashed blue lines show equation 14 and the dotted lines are equation 13, computed using seismic efficiency $\epsilon_s = 10^{-4}$ and with seismic source time parameter $X_s = 2$. Blue dot-dashed line, line of diamonds and shaded areas show similar heights but for $0.001R$. The wide pink lines shows the catastrophic disruption threshold as a function of asteroid diameter, computed using Eq. (3) by Jutzi et al. (2010) and coefficients for pumice from their Table 3. Two lines are shown on the left, the upper line shows a curve for a body with strength and the lower curve for rubble. Two lower lines (thin green, and thicker grey) give minimum impactors capable of causing global seismic shaking (GS) or seismic waves with accelerations greater than the surface gravity. These are computed using equation 9 by Richardson et al. (2005) and are computed for seismic frequencies 10 and 100 Hz.

25

blue lines, shaded in darker blue, boulders with height $h_{\text{boulder}} > 0.001R$ could be stranded on the surface by a seismic pulse. We have assumed a seismic efficiency $\epsilon_s = 10^{-4}$ (a relatively large value), density $\rho = 1$ g/cm^3, projectile velocity $V_{\text{proj}} = 5$ km/s (typical of asteroid collisions; Bottke et al. 1994), and a seismic source time parameter $X_s = 2$.

Catastrophic disruption and global reverberation thresholds for impacts are also shown in Figure 9. The wide pink lines shows the catastrophic disruption thresholds as a function of asteroid diameter, computed using Eq. (3) by Jutzi et al. (2010) and coefficients for pumice from their Table 3. Two lines are shown at the top. The upper one shows a body with strength and the lower curve extends the gravity regime for a rubble asteroid. Assuming a single seismic wave frequency, Richardson et al. (2005) estimated the diameter of a projectile D_{proj} (their equation 15) sufficient to cause seismic vibration across the whole body that is above the surface gravitational acceleration. We show this global seismicity threshold as a thin green line for a seismic frequency of 10 Hz and as a thicker grey line for a frequency of 100 Hz. For these curves, we assume P-wave velocity $V_p = 100$ m/s, typical of lunar regolith, attenuation coefficient $Q = 2000$ and seismic diffusivity $K_s = 0.1$ km^{2}s^{-1}.

Figure 9 shows that larger impacts that are just below the catastrophic disruption threshold are capable of ejecting moderate depths of surface material via excitation of a seismic pulse. In the darker orange region, boulders larger than 1/100th the radius of the asteroid can emerge to the surface after the seismic pulse ejects material off the surface. To eject surface material, the acceleration provided by the pulse once it reaches the surface must be greater than the net gravity at that point. The shaded regions lie above the acceleration dependent global seismicity thresholds previously estimated by Richardson et al. (2005) and so accelerations in the seismic pulse should satisfy this condition.

In Figure 9 we chose seismic source time with $X_s = 2$. Larger X_s move the point where yellow dotted and dashed lines cross upward and to the right on the plot. The two lines cross because equation 13 has projectile diameter inversely proportional to source time parameter X_s whereas in equation 14 the diameter is $\propto X_s^{\frac{1}{2}}$. For boulder stranding via impact excited seismic pulses to be a relevant process on asteroids, Figure 9 suggests that the seismic source must satisfy $X_s \sim 1$. With $X_s \sim 1$ then the time for the pulse to travel the diameter of the projectile is equal to the inverse pulse duration.

The time is longer than seen in some laboratory experiments (Yasui et al., 2015) and numerical simulations (Güldemeister and Wünnemann, 2017) but shorter than computed via scaling estimates (used by Lognonné et al. 2009).

Figure 9 shows requirements for boulder stranding at the antipode of an impact site. Smaller impactors could strand the same size boulder nearer the impact side. However we have not taken into account attenuation of the seismic pulse as it travels through the asteroid but have allowed the energy of the pulse to spread out as a function of inverse distance. Pulse broadening and attenuation would increase the size of an impactor needed to strand a particular width of boulder on the surface. Figure 9 shows that boulder stranding could only be accomplished by large and energetic impactors. A catastrophic impact that produced a cloud of debris could also leave large boulders on the surface as ejecta re-accumulates.

3.1. Ejecta Mass Fraction

In this subsection we compare the fraction of mass that falls onto an asteroid surface as crater ejecta to that which could be lofted off the surface from a impact generated seismic pulse. Both could be sources of material that is ballistically sorted upon landing.

Impact craters on a "rubble pile" asteroid may be in or near a gravity-scaling regime (Holsapple, 1993; Asphaug et al., 2002). For our order of magnitude analysis we assume an asteroid in the gravity-scaling regime. Scaling relations for crater ejecta by Housen and Holsapple (2011) (summarized in their Table 1 and with coefficients in their Table 3) describe mass in the ejecta as a function of position (their equation 16), total mass ejected during crater formation (just above their equation 17), and velocity of ejecta as a function of position (their equation 9 in the gravity regime). Together these give an estimate for the total mass in ejecta with velocities above the escape velocity $M(v > v_{\mathrm{escape}})$ during formation of a crater. In units of the total ejected mass M_{crater}, the fraction of crater ejecta mass that escapes the asteroid

$$\frac{M(v > v_{\mathrm{escape}})}{M_{\mathrm{crater}}} \approx \left(\frac{D}{D_{\mathrm{crater}}}\right)^{-\frac{3\mu}{2}} \tag{15}$$

with $M_{\mathrm{crater}} \sim 0.3\rho R_{\mathrm{crater}}^3$. The fraction of ejecta mass that falls back onto the surface in units of asteroid mass is

$$f_{\mathrm{crater}} \sim \frac{M_{\mathrm{crater}} - M(v > v_{\mathrm{escape}})}{M} \sim 0.07 \left(\frac{D_{\mathrm{crater}}}{D}\right)^3 \left(1 - \left(\frac{D}{D_{\mathrm{crater}}}\right)^{-\frac{3\mu}{2}}\right).$$
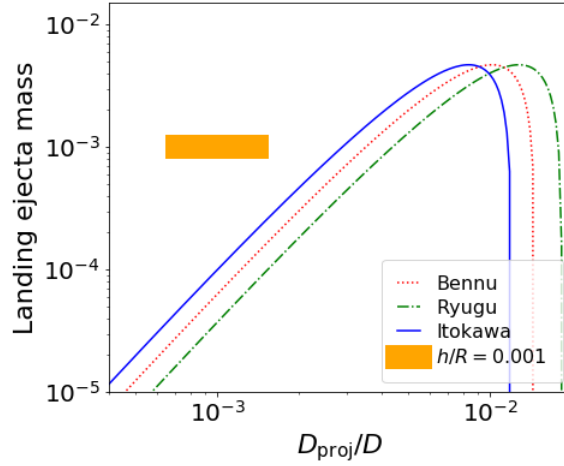
Figure 10: The fraction of crater ejecta mass in units of asteroid mass as a function of asteroid to projectile diameter ratio that is ejected below the escape velocity and returns to the asteroid surface. This fraction is computed with equation 16 based on scaling relations by Housen and Holsapple (2011) and for three different diameter asteroids. The blue solid, red dotted and green dot-dashed lines show the fraction for asteroids with the diameter of Ryugu, Bennu and Itokawa, respectively. The curves are computed with asteroid and projectile density $\rho = 1$ g/cm^3, and projectile velocity $V_{\mathrm{proj}} = 5$ km/s. The orange bar shows a rough estimate for mass ejected due to a seismic pulse that originates from a strong but sub-catastrophic impact with mean ejecta depth $h/R = 0.001$. This orange bar assumes that the impact lies in the blue and orange areas shown in Figure 9. If seismic pulses launched from impacts are strong enough to strand boulders on the surface, then they could dominate over crater ejecta as a source of ballistically sorted material.

The diameter of the crater D_{crater} can be estimated from the projectile diameter using the scaling estimate for crater radius in the gravity regime (also by Housen and Holsapple 2011)

$$\frac{D_{\text{crater}}}{D_{\text{proj}}} \sim \left(\frac{V_{\text{grav}}^2}{V_{\text{proj}}^2} \frac{D_{\text{proj}}}{D} \right)^{-\frac{\mu}{2+\mu}}. \tag{16}$$

In Figure 10 we show the fraction of returning crater ejecta mass in units of asteroid mass computed with equation 16 as a function of asteroid to projectile diameter ratio. The three curves give the fraction of mass in crater ejecta below the escape velocity. The blue solid, red dotted and green dot-dashed lines show the fraction for asteroids with the diameter of Ryugu, Bennu and Itokawa, respectively. The curves are computed with asteroid and projectile density $\rho = 1$ g/c^3, and projectile velocity $V_{\text{proj}} = 5$ km/s and exponent $\mu = 0.4$ following Table 3 by Housen and Holsapple (2011). Catastrophic impacts diameter ratio $D_{\text{proj}}/D \sim 10^{-2}$ (see Figure 9). For reference, the regime of strong but subcatastrophic impacts with $D_{\text{proj}}/D \sim 10^{-2}$ has a fraction of ejecta mass that falls back to the surface $f_{\text{crater}} \sim 10^{-4}$.

We now compare f_{crater} to the mass that is launched by a seismic pulse. The mass fraction of material lofted via an impact excited seismic pulse is $\sim h/R$ where h is the depth of material ejected averaged over the surface. We found in section 3 that with seismic source time parameter $X_s \sim 1$, a strong but sub-catastrophic impact might launch a depth $h/R \sim 0.01 - 0.001$. We place an orange bar on Figure 10 for a mass fraction of $h/R = 0.001$ for a strong but sub-catastrophic impact with $D_{\text{proj}}/D \sim 10^{-3}$. The orange bar lies above the mass fraction in crater ejecta. If seismic pulses launched from impacts are strong enough to uncover or strand boulders on the surface, then they could dominate over crater ejecta as a source of ballistically sorted material.

4. Summary

We have carried out laboratory experiments of impacts into polydisperse granular media, but focusing on impacts from below to mimic the behavior of an impact excited seismic pulse reaching the surface of an asteroid. Our laboratory impacts are strong enough that particles near and on the surface are ejected into the air. The viscoelastic soft sphere simulations by Tancredi et al. (2012) showed that a strong pressure pulse excited by an impact

would eject particles from an asteroid surface, and our experiments mimic this process.

We find that initially buried larger particles are often left on the surface after impact. Using particle image velocimetry of high speed video we measure ejecta velocities, finding that nearby particles have similar velocities. The time dependent ejecta velocity field is qualitatively different from crater ejecta curtains where there is a range of ejecta velocities and strong correlations (and scaling relations) between ejecta velocity, launch position and time (e.g., Housen and Holsapple 2011). We find that our ejecta trajectories are independent of particle size until they land. Collisions primarily take place upon landing and small particles scatter off of larger ones, leaving larger particles on the surface.

The tendency for falling smaller particles to scatter and leave larger particles on the surface has been dubbed 'ballistic sorting' by Shinbrot et al. (2017) who proposed that ballistic sorting of impactors could account for large boulders seen on the surfaces of rubble asteroids. Similarly we propose that ballistic sorting of ejecta launched by an impact generated seismic pulse can strand boulders on an asteroid surface. Our experiments show that a single pulse can strand a previously buried large particle. We have found that multiple pulses (but separated in time) continue to unearth larger particles and once a larger particle is on the surface it tends to stay there.

If seismic energy is rapidly attenuated in rubble asteroids then seismic reverberation may be short and ineffective. Boulder stranding of ejecta gives an attractive mechanism accounting for large boulders on the surface of asteroids. Most mechanisms that produce the Brazil nut effect are effective at low surface gravity but have longer time scales with decreased surface gravity (Maurel et al., 2017; Chujo et al., 2018). However, seismic pulses might be effective in low surface gravity environments because they can eject more material off the surface. Future low gravity experiments and simulations might explore this possibility. While we have primarily considered sub-catastrophic impacts, ballistic sorting might happen following catastrophic disruption by an impact and during a phase of re-accumulation. Stress failure following spin-up might also eject equatorial material (e.g., Sanchez and Scheeres 2018; Yu et al. 2018) that could ballistically sort during a phase of re-accumulation.

Using seismic efficiency and source time parameters we explored the regime where an impact generated seismic pulse could strand large boulders on the surface of a rubble asteroid such as Bennu or Ryugu. Our experiments suggested that boulder stranding is likely to take place if the acceleration in

30

the seismic pulse is be above that of surface gravity, the ejected material reaches a height above the surface larger than the boulder height, and the depth of ejected material is larger than the boulder height. For a single impact to leave a large boulder stranded on the surface, we find that the impact must be nearly catastrophic, the seismic efficiency must be fairly high, $\sim 10^{-4}$, and the seismic pulse duration must be similar to the sound travel time across the distance of the projectile diameter.

A single impact excited seismic pulse would be strongest on the surface nearest the impact (Thomas and Robinson, 2005) and so boulder stranding by a seismic pulse might give larger boulders near an impact site. A single impact would be expected to cause an inhomogeneous surface size distribution or one that varies as a function of position on the surface. If the size particle distribution does not vary with position on the surface (e.g. as suggested by observations of 4179 Toutatis; Jiang et al. 2015), then one might rule out this process as an explanation for large surface boulders, and we might place constraints on the nature of seismic pulse propagation in the interior.

The mechanism for boulder stranding explored here may not explain the correlation of large and small boulders being distributed into regions of high and low potential observed on Itokawa (Miyamoto et al., 2007; Tancredi et al., 2015). Our process is dependent on the there being large boulders below the surface before a subsurface pulse ejects material. If there are no large boulders below the surface of the low potential regions then only smaller boulders will be present and we are not able to distinguish our process compared to others. However, if there are large boulders present below the surface when material is ejected then our experiments have shown that smaller particles will scatter off large particles during landing. It is possible that when material is ejected off the surface of Itokawa the smaller boulders will scatter into low potential regions leaving larger boulders in the high potential regions. Our mechanism cannot fully explain the correlation of the boulder size distribution with potential on Itokawa suggesting size segregation processes on asteroids likely include more than one mechanism.

4.1. Role of microgravity and atmosphere

Our experiments are carried out under the gravitational and atmospheric conditions of Earth (one atmosphere of pressure and 1g) and so do not necessarily mimic conditions or materials on an asteroid. A milli, or micro, gravity environment would reduce the strength of a pulse required to eject surface particles and would prolong their time of flight. However lower gravity would

also affect the strength of hydrostatic forces and so how the pulse propagates through the medium. Any size segregation due to the Brazil Nut effect would still occur, but take a longer time for lower surface gravities.

As particles can be ejected at lower velocities in reduced-gravity environments, collisions between particles upon landing would also be less energetic. If the coefficient of restitution is higher than in our experiments, particles would travel further after scattering facilitating boulder stranding.

As evidenced by the sample from asteroid Itokawa, asteroid regolith is likely to contain very fine particles (dust). In our experiments however, we have deliberately removed these particles in order to mitigate the role of attenuation caused by air drag. Additionally, the presence of dust would necessarily introduce cohesive forces into the dynamics of the system, something we have neglected so that we can identify and understand the main mechanism behind our experimental results and their application to asteroids.

We have also neglected attenuation of a seismic pulse when estimating a regime for boulder stranding on an asteroid, but let the energy spread out as the inverse distance squared. However, attenuation and scattering probably would broaden the pulse and reduce its amplitude. The shape of the pulse through time, the wave speed as a function of depth in the asteroid, the pulse arrival time, and strength at different locations on the surface, would also influence the ejecta velocity distribution and should be investigated. However, we have left them out of this first set of experiments and analysis in order to maintain their simplicity. Future research will attempt to include all these other variables and study their influence.

———————————— References

References

Allan, D., Caswell, T., Keim, N., van der Wel, C., August 2016. Trackpy v0.3.2.
URL https://doi.org/10.5281/zenodo.60550

Asphaug, E., 2008. Critical crater diameter and asteroid impact seismology. Meteoritics & Planetary Science 43 (6), 1075–1084.

Asphaug, E., Ryan, E., T. Zuber, M., 01 2002. Asteroid Interiors.

Bottke, W. F., Nolan, M., Greenberg, R., Kolvoord, R., 1994. Velocity distributions among colliding asteroids. Icarus 107, 255–268.

Cheng, A., Izenberg, N., Chapman, C., Zuber, M. T., 2002. Ponded deposits on asteroid 433 eros. Meteoritics & Planetary Science 37, 1095–1105.

Chujo, T., Mori, O., Kawaguchi, J., Yano, H., 2018. Categorization of brazil nut effect and its reverse under less-convective conditions for microgravity geology. Monthly Notices of the Royal Astronomical Society, 474 (4), 4447–4459.

Cintala, M. J., Head, J. W., Veverka, J., 1978. Characteristics of the cratering process on small satellites and asteroids. Proceedings of Lunar Sci. Conf. 9, 3803–3830.

Clement, C. P., Pacheco-Martinez, H. A., Swift, M. R., King, P. J., sep 2010. The water-enhanced brazil nut effect. EPL (Europhysics Letters) 91 (5), 54001.
URL https://doi.org/10.1209%2F0295-5075%2F91%2F54001

Crocker, J. C., Grier, D. G., 1996. Methods of digital video microscopy for colloidal studies. Journal of Colloid Interface Science 179, 298–310.

Dainty, A., Toksöz, M. N., Anderson, K., Pines, P., Nakamura, Y., Latham, G., 1974. Seismic scattering and shallow structure of the moon in oceanus procellarum. Moon 9, 11–29.

Greenberg, R., Bottke, W., M., N., Geissler, P., Petit, J., Durda, D., Asphaug, E., Head, J., 1996. Collisional and dynamical history of ida. Icarus 120, 106–118.

Greenberg, R., Nolan, M., Bottke, W., Kolvoord, R., Veverka, J., 1994. Collisional history of gaspra. Icarus 107, 84–97.

Güldemeister, N., Wünnemann, K., 2017. Quantitative analysis of impact-induced seismic signals by numerical modeling. Icarus 296, 15–27.

Herrmann, H. J., Hovi, J. P., Luding, S. (Eds.), 1997. Physics of Dry Granular Media. Vol. Vol. 350 of NATO ASI Series. Kluwer Academic Publishers, Dordrecht.

Hirata, N., Nakamura, A. M., 2006. Secondary craters of tycho: Size-frequency distributions and estimated fragment size-velocity relationships. Journal of Geophysical Research 111 (E3), E03005.

Hoerth, T., Schafer, F., Nau, S., Kuder, J., Poelchau, M. H., Thoma, K., Kenkmann, T., 2014. In situ measurements of impact-induced pressure

waves in sandstone targets. Journal of Geophysical Research Planets 119, 2177–2187.

Holsapple, K. A., 1993. The scaling of impact processes in planetary sciences. Annual Review of Earth and Planetary Sciences 21, 333–373.

Hong, D. C., Quinn, P. V., Luding, S., 2001. Reverse brazil nut problem: Competition between percolation and condensation. Physics Review Letters 86 (15), 3423–3426.

Housen, K. R., Holsapple, K. A., 2011. Ejecta from impact craters. Icarus 211, 856–875.

Jiang, Y., Ji, J., Huang, J., Marchi, S., Li, Y., Ip, W.-H., 11 2015. Boulders on asteroid toutatis as observed by chang'e-2. Scientific Reports 5, 16029 EP.

Jullien, R., Meakin, P., Pavlovitch, A., 1992. Three-dimensional model for particle-size segregation by shaking. Physical Review Letters 69 (4), .640–643.

Jutzi, M., Michel, P., Benz, W., Richardson, D. C., 2010. Fragment properties at the catastrophic disruption threshold: The effect of the parent body's internal structure. Icarus 207, 54–65.

Knight, J., Jaeger, H., Nagel, S., 1993. Vibration-induced size separation in granular media: The convection connection. Physics Review Letters 70, 3728–3731.

Latham, G. V., McDonald, W. G., Moore, H. J., 1970. Missile impacts as sources of seismic energy on the moon. Science 168 (3928), 242–245.

Lognonné, P., Feuvre, M. L., Johnson, C. L., Weber, R. C., 2009. Moon meteoritic seismic hum: steady state prediction. Journal Geophysical Research (Planets) 114, 12003.

Makse, H. A., Gland, N., Johnson, D. L., Schwartz, L., 2004. Granular packings: Nonlinear elasticity, sound propagation, and collective relaxation dynamics. Physical Review E 70, 061302.

Matsumura, S., Richardson, D. C., Michel, P., Schwartz, S. R., Ballouz, R.-L., 2014. The brazil nut effect and its application to asteroids. Monthly Notices of the Royal Astronomical Society 443, 3368–3380.

Maurel, C., Ballouz, R.-L., Richardson, D. C., Michel, P., Schwartz, S. R., 2017. Numerical simulations of oscillation-driven regolith motion: Brazil-nut effect. Monthly Notices of the Royal Astronomical Society 464, 2866–2881.

McGarr, A., Latham, G., Gault, D., 1969. Meteoroid impacts as sources of seismicity on the moon. Journal of Geophysical Research 74, 5981–5994.

Meakin, P., Ramanlal, P., Sander, L. M., Ball, R. C., 1986. Ballistic deposition on surfaces. Physical Review A 34, 5091.

Melosh, H. J., 1989. Impact cratering: a geologic process. Oxford Monographs on Geology and Geophysics. Oxford University Press, Oxford England.

Miyamoto, H., Yano, H., Scheeres, D. J., Abe, S., Barnouin-Jha, O., Cheng, A. F., Demura, H., Gaskell, R. W., Hirata, N., Ishiguro, M., Michikami, T., Nakamura, A. M., Nakamura, R., Saito, J., Sasaki, S., May 2007. Regolith migration and sorting on asteroid itokawa. Science 316 (5827), 1011–1014.

Möbius, M. E., Cheng, X., Eshuis, P., Karczmar, G. S., Nagel, S. R., Jaeger, H. M., Jul 2005. Effect of air on granular size separation in a vibrated granular bed. Phys. Rev. E 72, 011304.
URL https://link.aps.org/doi/10.1103/PhysRevE.72.011304

Nakamura, Y., 1976. Seismic energy transmission in the lunar surface zone determined from signals generated by movement of lunar rovers. Bulletin of the Seismological Society of America 66 (2), 593–606.

Naylor, M. A., Swift, M. R., King, P. J., Jul 2003. Air-driven brazil nut effect. Phys. Rev. E 68, 012301.
URL https://link.aps.org/doi/10.1103/PhysRevE.68.012301

Nolan, M. C., Asphaug, E., Greenberg, R., Jun. 1992. Numerical Simulation of Impacts on Small Asteroids. In: AAS/Division for Planetary Sciences Meeting Abstracts #24. Vol. 24 of Bulletin of the American Astronomical Society. p. 959.

O'Donovan, J., Ibraim, E., O'Sullivan, C., Hamlin, S., Wood, D. M., Marketos, G., 2016. Micromechanics of seismic wave propagation in granular materials. Granular Matter 18, 56.

Perera, V., Jackson, A. P., Asphaug, E., Ballouz, R.-L., 2016. The spherical brazil nut effect and its significance to asteroids. Icarus 278, 194–203.

Richardson, J. E., Melosh, H. J., Greenberg, R., 2004. Impact-induced seismic activity on asteroid 433eros: A surface modification process. Science 306, 1526–1529.

Richardson, J. J., Melosh, H. J., Greenberg, R. J., O'Brien, D. P., 2005. The global effects of impact-induced seismic activity on fractured asteroid surface morphology. Icarus 179, 325–349.

Rosato, A., Strandburg, K. J., Prinz, F., Swendsen, R. H., 1987. Why the brazil nuts are on top: Size segregation of particulate matter by shaking. Physics Review Letters 58, 1038–1042.

Sánchez, P., Scheeres, D. J., May 2014. The strength of regolith and rubble pile asteroids. Meteoritics & Planetary Science 49 (5), 788–811.

Sanchez, P., Scheeres, D. J., 2018. Rotational evolution of self-gravitating aggregates with cores of variable strength. Planetary and Space Science 157, 39–47.

Scheeres, D. J., Sanchez, P., 2018. Implications of cohesive strength in asteroid interiors and surfaces and its measurement. Progress in Earth and Planetary Science 5, 25.

Schultz, P. H., Gault, D. E., 1975. Seismic effects from major basin formations on the moon and mercury. Moon 12, 159–177.

Shinbrot, T., Sabuwala, T., Siu, T., Lazo, M. V., Chakraborty, P., 2017. Size sorting on the rubble-pile asteroid, itokawa,. Physics Reviews Letters 118, 111101.

Shishkin, N. I., 2007. Seismic efficiency of a contact explosion and a high velocity impact. Journal of Applied Mechanics and Technical Physics 48, 145–152.

Tancredi, G., Maciel, A., Heredia, L., Richeri, P., Nesmachnow, S., 2012. Granular physics in low-gravity environments using discrete element method. Monthly Notices of the Royal Astronomical Society 420, 3368–3380.

Tancredi, G., Roland, S., Bruzzone, S., 2015. Distribution of boulders and the gravity potential on asteroid itokawa. Icarus 247, 279–290.

Thomas, P. C., Robinson, M. S., 2005. Seismic resurfacing by a single impact on the asteroid 433 eros. Nature 436, 366–369.

Titley, S. R., 1966. Seismic energy as an agent of morphologic modification on the moon. Tech. rep., United States Geological Survey, Flagstaff, AZ.

Toksöz, M. N., Dainty, A. M., Solomon, S., Anderson, K., 1974. Structure of the moon. Reviews of Geophysics 12 (4), 539–567.

Williams, J., 1976. The segregation of particulate materials. a review. Powder Technology 15 (2), 245–251.

Wolf, A., 1944. The equation of motion of a geophone on the surface of an elastic earth. Geophysics 9, 29–34.

Yamada, T. M., Ando, K., Morota, T., Katsuragi, H., 2016. Timescale of asteroid resurfacing by regolith convection resulting from the impact-induced global seismic shaking. Icarus 272, 165–177.

Yasui, M., Matsumoto, E., Arakawa, M., 2015. Experimental study on impact-induced seismic wave propagation through granular materials. Icarus 260, 320–331.

Yu, Y., Michel, P., Hirabayashi, M., Schwartz, S. R., Zhang, Y., Richardson, D. C., Liu, X., 2018. The dynamical complexity of surface mass shedding from a top-shaped asteroid near the critical spin limit. Astronomical Journal 156, 59–77.